

Continuous and Time-Domain Coherent Signal Conversion between Optical and Microwave Frequencies

G.A. Peairs^{1,2}, M.-H. Chou^{2,3}, A. Bienfait^{2,†}, H.-S. Chang², C.R. Conner², É. Dumur^{2,4,‡}, J. Grebel², R.G. Povey^{2,3}, E. Şahin², K.J. Satzinger^{1,2,§}, Y.P. Zhong² and A.N. Cleland^{2,4,*}

¹*Department of Physics, University of California, Santa Barbara, California 93106, USA*

²*Pritzker School of Molecular Engineering, University of Chicago, Chicago, Illinois 60637, USA*

³*Department of Physics, University of Chicago, Chicago, Illinois 60637, USA*

⁴*Argonne National Laboratory, Argonne, Illinois 60439, USA*

 (Received 14 May 2020; revised 1 October 2020; accepted 2 November 2020; published 4 December 2020)

A quantum network consisting of computational nodes connected by high-fidelity communication channels could expand information-processing capabilities significantly beyond those of classical networks. Superconducting qubits hold promise for scalable and high-fidelity quantum computation at microwave frequencies but must operate in an isolated cryogenic environment, obviating the potential for practical long-range communication. Quantum communication has, however, been demonstrated with optical photons. A fast efficient quantum-coherent interface between superconducting qubits and optical photons would provide a key resource for a large-scale quantum network or distributed quantum computer. Here, we describe the design and experimental operation of a device incorporating a silicon optomechanical nanobeam combined with an aluminum-nitride-based electromechanical transducer. We experimentally demonstrate classical continuous-wave operation of this device at room temperature with external conversion efficiencies of $(2.5 \pm 0.4) \times 10^{-5}$ (microwave to optical) and $(3.8 \pm 0.4) \times 10^{-5}$ (optical to microwave), corresponding to internal efficiencies of 2.4% and 3.7%, respectively. This device also has a larger bandwidth than previous efficient microwave-optical transducers, allowing us to operate in the time domain with 20-ns pulses.

DOI: [10.1103/PhysRevApplied.14.061001](https://doi.org/10.1103/PhysRevApplied.14.061001)

Recent experiments have demonstrated high-fidelity operation of increasingly complex microwave-frequency superconducting qubits [1,2]. A microwave-optical transducer would enable a quantum optical network with superconducting nodes, allowing quantum communication or distributed computation beyond a single dilution refrigerator [3–6]. One approach to microwave-optical transduction uses mechanical motion as an interface between the two electromagnetic frequencies [7–13]. While high efficiencies have been achieved using resonant mechanical modes with frequencies around 1 MHz [14], transfer rates faster than a typical qubit lifetime of order $1 \mu\text{s}$ are much desired. Microwave-frequency mechanical approaches are highly attractive, as is underlined by recent developments

in quantum electromechanics and optomechanics demonstrating quantum control of such modes [15–20].

If a mechanical mode near 5 GHz is used as the interface, this can be cooled to its ground state in a dilution refrigerator, allowing state transfer with less than one phonon of added noise [21]. These mechanical modes can also yield large transduction bandwidths.

Silicon-based optomechanics support mechanical modes at gigahertz frequencies with high-quality factors and optomechanical coupling to infrared light [22–24]. Previous experiments have demonstrated bidirectional conversion between microwaves and optics using piezo-optomechanics in an aluminum nitride (AlN) optomechanical device [10]. More recent experiments have demonstrated piezo-optomechanical transduction using a mechanical oscillator in its quantum ground state [11] as well as bidirectional transduction [12].

Here, we describe an aluminum-nitride-based interdigital transducer (IDT) with a silicon-based optomechanical resonator, which promises the necessary coupling rates to efficiently convert signals between infrared and microwave frequencies. We demonstrate room-temperature bidirectional conversion of continuous-wave

*anc@uchicago.edu

†Present address: Université de Lyon, ENS de Lyon, Université Claude Bernard, CNRS, Laboratoire de Physique, F-69342 Lyon, France.

‡Present address: Université Grenoble Alpes, CEA, INAC-Pheliqs, 38000 Grenoble, France.

§Present address: Google, Santa Barbara, California 93117, USA.

signals with an internal efficiency above 1% and a transduction bandwidth above 3 MHz, as well as time-domain operation on short time scales.

In Fig. 1, we display the device design and operation, comprising an $80 \times 80 \mu\text{m}^2$ Si membrane that includes an AlN piezoelectric layer overlaid by an interdigitated transducer (IDT). This converts between a microwave electrical signal near 4.7 GHz and a symmetric Lamb-wave acoustic mode (mode \hat{c} , frequency $\Omega_{\text{em}} = 4.7$ GHz) with coupling rate $\gamma_{c,e}$. The mechanical Lamb waves are directed at one end of a nanobeam optomechanical crystal [25], with the hole pattern allowing Lamb waves to pass to the central optomechanically active part of the structure, where strong interactions occur between the localized mechanical mode at $\Omega_m = 4.7$ GHz (mode \hat{b} , coupled to the Lamb mode \hat{c} with rate G_{me}) and a localized optical mode at $\omega_{\text{opt}} = 194$ THz (mode \hat{a} , with single-photon coupling g_0 to the mechanical mode \hat{b}). The optical mode has extrinsic coupling $\kappa_e/2$ to each of two propagation directions in an evanescently coupled waveguide. The intrinsic dissipation rates are κ_i , $\gamma_{b,i}$, and $\gamma_{c,i}$ and the cavity loss rates $\kappa = \kappa_i + \kappa_e$, $\gamma_b = \gamma_{b,i}$, and $\gamma_c = \gamma_{c,i} + \gamma_{c,e}$. The optomechanical coupling is $\sqrt{n_{\text{opt}}}g_0$ when the optical cavity has n_{opt} photons [26]. The detailed design of the optical elements and coupling are very similar to earlier work [10].

We use a laser as the optical pump, detuned from the cavity by $\Delta \equiv \omega_{\text{opt}} - \omega_{\text{pump}} \sim \pm\Omega_m$. This pump carries sidebands at $\omega_{\text{pump}} \pm \Omega$ (Ω is the microwave signal frequency). We treat the sideband nearest the optical resonance as the signal and consider transduction between that sideband and the electrical port of the device. The off-resonant sideband interferes with this transduction, which we model to estimate the signal tone conversion.

We define the external microwave-to-optical transduction efficiency η_{ext} as the ratio between the average output optical photon rate in the near-resonant sideband and the average input microwave photon rate, where the output refers to the optical fiber above the device chip, coupled through a grating coupler to the evanescently coupled waveguide, and the input refers to the microwave cable before the chip. The optical-to-microwave efficiency is defined in the reverse manner. Ideally, this would be equal to the microwave-to-optical efficiency but as there are a number of spurious mechanical modes that are not excited in this reverse process, this is not necessarily so.

The efficiency depends on the parameters (Ω , Δ , n_{opt}); we define the constant-pump transduction bandwidth as the 3-dB bandwidth of η in signal frequency Ω , for a given pump detuning Δ and optical-cavity population n_{opt} . We can factor out the dependence of η_{ext} on these operating

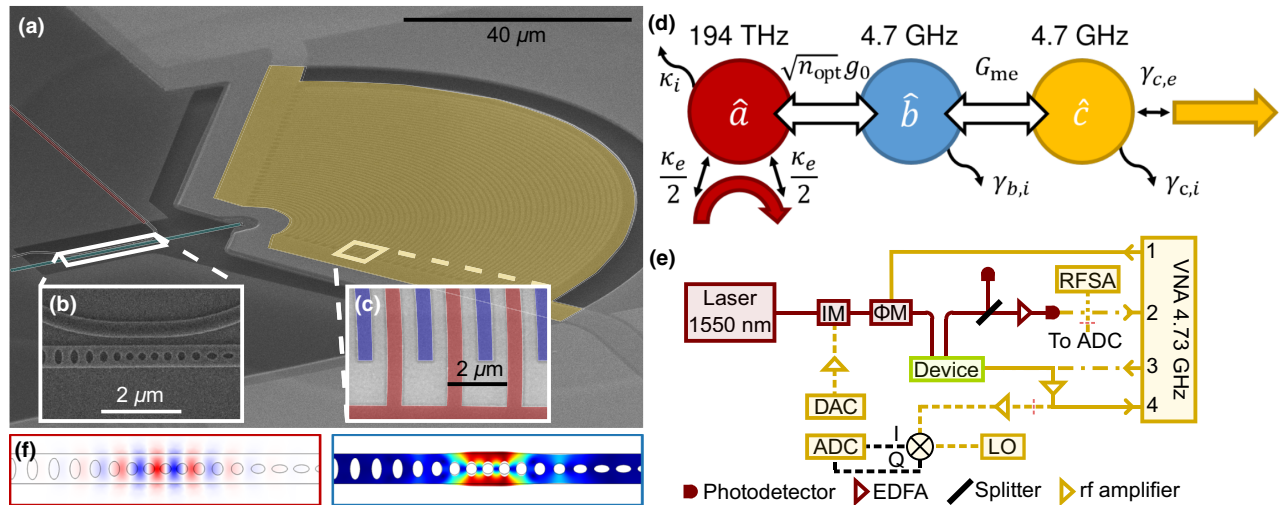


FIG. 1. The experimental setup and device. (a) A false-color scanning electron micrograph of the microwave-optical transducer, including the photonic waveguide (red), optomechanical nanobeam (blue), and interdigitated transducer (yellow). Inset (b) shows the optomechanical nanobeam and the coupling waveguide pattern. Inset (c) shows the interdigitated transducer, with signal (red) and ground (blue) electrodes, in phase with the strain and voltage pattern of the electromechanical mode \hat{c} . (d) A schematic representation of the transduction model. The optical mode corresponds to \hat{a} , the localized mechanical mode to \hat{b} , and the membrane electromechanical mode to \hat{c} . (e) A simplified measurement schematic, with microwave components in yellow and optical components in red. The solid lines are for continuous-wave optical-to-microwave transduction and the dashed-dotted lines are additional pathways for other measurements. IM, intensity modulator; PM, phase modulator; RFSAs, rf spectrum analyzer; LO, local oscillator; DAC, digital-to-analog converter; ADC, analog-to-digital converter. (f) Simulated optical (\hat{a} , left) and mechanical (\hat{b} , right) mode patterns in the center of the optomechanical structure.

parameters:

$$\eta_{\text{ext}}(\Omega, \Delta, n_{\text{opt}}) = \eta_{\text{chip}} \eta_o \eta_e \eta_{\text{int}}(\Omega, \Delta, n_{\text{opt}}), \quad (1)$$

where $\eta_o \equiv (\kappa_e/2)/\kappa$ and $\eta_e \equiv \gamma_{c,e}/\gamma_c$ are the optical and electrical external coupling ratios, $\eta_{\text{chip}} = 0.25$ is the power efficiency of coupling signals between the device chip and an optical fiber, achieved using grating couplers, and η_{int} is the “internal” transduction efficiency.

For operation with a red-detuned pump, the maximum value of η_{int} is 1, while amplification can be achieved with a blue-detuned pump at the cost of added noise [27]. Because of our two-sided coupling to the optical resonance, η_o for this device includes a factor of 1/2, limiting the ideal red-detuned η_{ext} to 0.5. For sideband-unresolved systems ($\kappa > \Omega_m$), there is also non-negligible transmission into (or from) the off-resonant sideband. For a scheme using both sidebands, the off-resonant sideband may cause interference.

The device in Fig. 1(a) is fabricated on a silicon-on-insulator substrate. A thin layer of SiO₂ protects the areas used for photonic components. A 330-nm film of AlN is uniformly deposited and patterned. The protective SiO₂ layer is then removed and the optical elements defined by electron-beam lithography followed by two photolithographic etching steps. The IDT is then patterned by aluminum liftoff. A release window is patterned and the nanobeam and IDT membrane mechanically released by HF vapor.

The optomechanical nanobeam is designed so that acoustic radiation is emitted in only one direction, with a

phonon leakage rate above 1 MHz without affecting the optomechanical coupling g_0 . The IDT has a finger pitch of approximately 1 μm , designed to couple to symmetric 4.7 GHz Lamb-like waves, adjusted by up to 2% as a function of the in-plane angle to correct for acoustic anisotropy [28].

The phononic waveguide connection to the electromechanical membrane is designed to minimize coupling to unwanted bilayer membrane modes. Besides the desired fundamental symmetric Lamb wave, there are also membrane shear modes and edge-guided modes. To reduce coupling to these modes, the nanobeam holes are tapered in size and the nanobeam widened to 1 μm and the nanobeam attaches to the membrane with a large opening angle. To reduce coupling to the antisymmetric Lamb-like mode, the AlN is patterned to create a 500-nm-long ramp between the bilayer and silicon. Finite-element simulations indicate that approximately 15% of the power radiating into the membrane goes into these unwanted modes.

Measurements are performed in ambient conditions, as shown in Fig. 1(e). The dc optical transmission displays an optical mode at 1548 nm with intrinsic loss $\kappa_i = 2\pi \times 3.8 \pm 0.4$ GHz and extrinsic loss $\kappa_e = 2\pi \times 6.5 \pm 0.3$ GHz. Thermomechanical noise generates a peak in the rf power spectrum, yielding a mode frequency of 4.737 GHz with full width at half maximum 6.2 ± 0.1 MHz and single-photon optomechanical coupling $g_0 = 2\pi \times 734 \pm 31$ kHz.

The electromechanical mode is characterized using microwave reflection measurements at the IDT, yielding a $\Omega_{\text{em}} = 4.737$ GHz resonance with total loss $\gamma_c =$

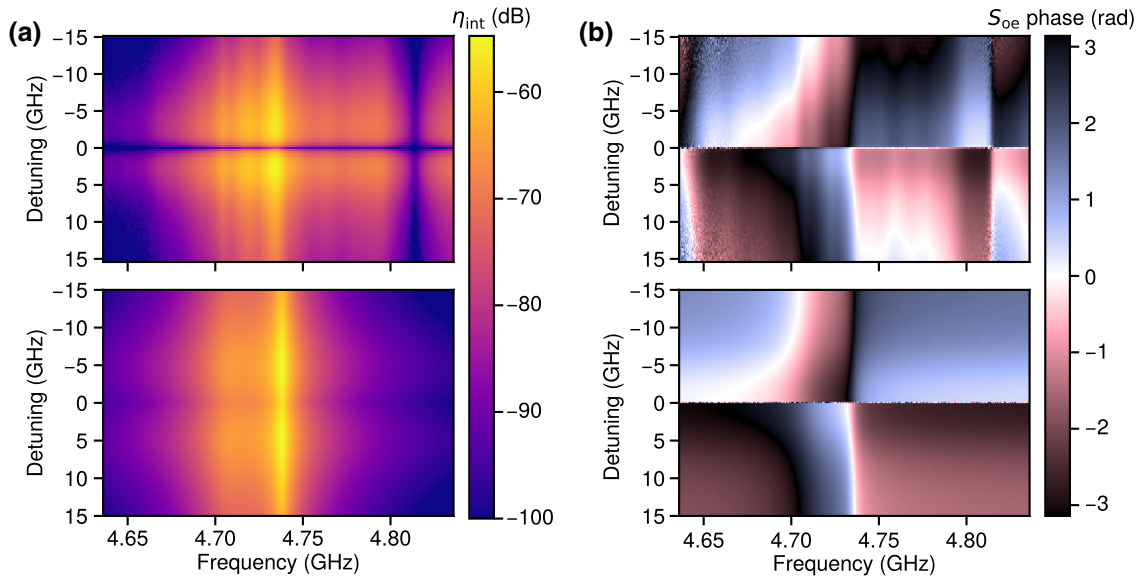


FIG. 2. Low-power microwave-to-optical transduction: above, experiment; below, theory, using independently fitted parameters. (a) The internal efficiency. (b) The scattering phase. The small modulations in the measured scattering-matrix element are due to microwave impedance mismatch and IDT coupling variations with frequency. The measurements are made at an optical power of 1.2 μW .

$2\pi \times 24.6 \pm 0.5$ MHz and external coupling to a 50Ω transmission line $\gamma_{c,e} = 2\pi \times 310 \pm 10$ kHz.

The coupling rate G_{me} between the nanobeam mechanics and the membrane electromechanics is not directly accessible; simulations imply $G_{me} = 2\pi \times 1.15$ MHz.

We characterize the bidirectional conversion efficiency using a continuous pump and signal. For microwave-to-optical transduction, we sweep a microwave signal through the operating frequency, detecting a beat in the transmitted optical power using a broadband photodetector, yielding the electrical-to-optical scattering matrix element S_{oe} . As shown in Fig. 2, we sweep a low-power laser wavelength across the optical resonance, observing the expected symmetric transduction for red and blue detuning, with a 3-dB bandwidth of 8.1 MHz.

The signal pathway is calibrated to convert this measurement into the external photon-number efficiency η_{ext} , plotted in Fig. 3(a) as a function of the pump power (blue points). Power-dependent red shifting of the optical

resonance prevents red-detuned operation at high powers, so η_{ext} is calculated in blue-detuned operation. We achieve a maximum external efficiency of $\eta_{ext} = (2.5 \pm 0.4) \times 10^{-5}$ with $168 \mu\text{W}$ in the input waveguide, with a 3-dB bandwidth of 3.4 MHz.

For optical-to-microwave transduction, we use a phase modulator to create sidebands on the input signal, considering only the near-resonant sideband to be the signal. We detect the out-coupled IDT microwave signal, converted to an external transduction efficiency η'_{ext} . The peak efficiency is plotted in Fig. 3(a) as a function of the pump power (orange points). We achieve a maximum of $\eta'_{ext} = (3.8 \pm 0.4) \times 10^{-5}$ at $231 \mu\text{W}$, with a 3-dB bandwidth of 3.8 MHz, in good agreement with the measured η_{ext} as with our model. The transmission is shown in Fig. 3(b) at optimal detuning.

To perform microwave-to-optical transduction in the time domain, we use an optical-intensity modulator to produce 20-ns rectangular optical pulses with rise and fall times of 5 ns and an on-off ratio of 23 dB. The IDT is driven continuously with a microwave source and the transmitted pulse in optical beat power detected with a fast photodiode. The resulting microwave signal is demodulated and both the in-phase I and out-of-phase Q quadratures are captured. By using laser wavelengths around the low-power-equilibrium resonant wavelength (see Fig. 4), we observe the time-dependent red shifting of the resonance, marked by the zero in transmission when the pump is resonant and the sidebands interfere destructively.

For red-detuned pump powers around $87 \mu\text{W}$, the optical mode shifts by approximately 5 GHz in 20 ns. Despite not operating at optimal detuning for the duration of a 20-ns pulse, we observe both red- and blue-detuned transduction. We calculate that approximately 1.6×10^{-6} (1.3×10^{-6}) of the input microwave photons in 20 ns are transduced when red (blue) detuned.

If we consider the blue-detuned continuous-wave efficiency in our model as a function of the power and integrate that efficiency over the pulse, we expect a total external efficiency of 8.1×10^{-6} . The lower observed efficiency may be attributed to the time-varying detuning, the finite transduction bandwidth of the device, and operation faster than mechanical amplification by the blue-detuned pump.

In summary, we demonstrate classical continuous-wave operation of a bidirectional microwave-optical converter at room temperature, with external conversion efficiencies of $\eta_{ext} = (2.5 \pm 0.4) \times 10^{-5}$ (microwave to optical) and $\eta'_{ext} = (3.8 \pm 0.4) \times 10^{-5}$ (optical to microwave), with a bandwidth exceeding 3 MHz. We also demonstrate pulsed-pump operation for phase-coherent transduction in the time domain.

A major factor limiting the external efficiency is the poor impedance matching of the IDT to a 50Ω transmission line, which gives a ratio of external coupling to total

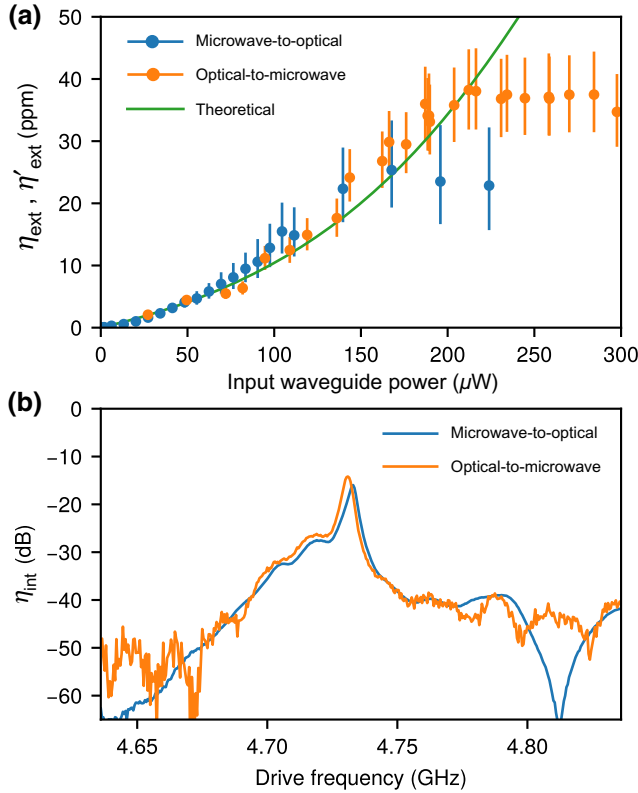


FIG. 3. Bidirectional transduction. (a) The pump-power dependence of the measured microwave-to-optical (blue) and optical-to-microwave (orange) external transduction efficiencies η_{ext} and η'_{ext} , respectively. The detuning is optimized at each point to maximize transduction. The error bars are 90% confidence intervals; the green curve is the theoretical efficiency using independently determined model parameters. (b) Microwave-to-optical (blue) and optical-to-microwave (orange) transduction at the optimized pump powers.

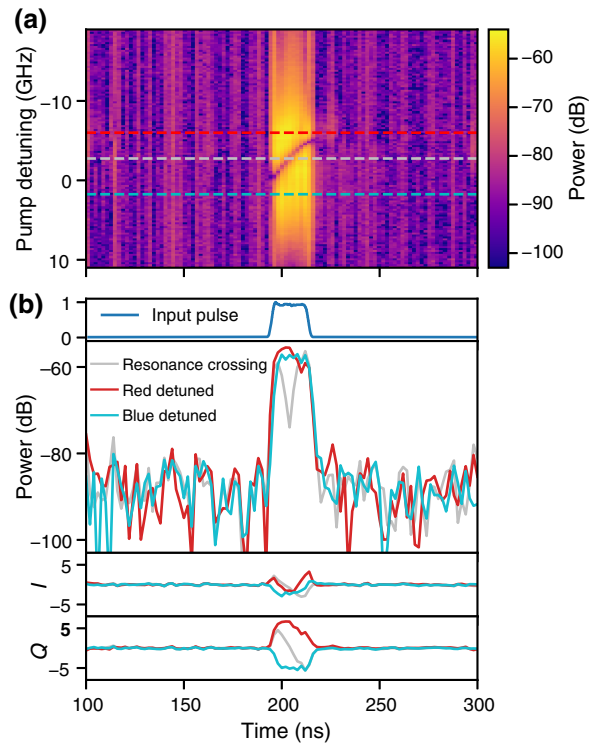


FIG. 4. Time-domain microwave-to-optical transduction. (a) The detected power over time for a range of initial pump detunings, referenced to external input signal pulse height. (b) The time traces (10^6 measurements averaged, $8\text{-}\mu\text{s}$ repetition rate) for pump probe pulse and (red) resonance-crossing and (blue) detuned pulses, using the corresponding dashed cut lines. The measured pulse approximately matches the input rectangular pulse with duration 20 and 5 ns (above), adjusted for a 194-ns travel time. The maximum input waveguide power during the pulse is $87\ \mu\text{W}$. Quadrature plots are shown on a linear scale at the bottom, in arbitrary units.

loss in the electromechanical resonator of $\eta_e = 0.013$. This ratio can be made close to 1 by impedance matching to the transducer [29]. Impedance matching, while relevant for classical measurements, is not relevant for quantum operation. Because η_o and η_{chip} can also be optimized without fundamentally changing the device itself, using Eq. (1), we calculate a microwave-to-optical internal efficiency of 2.4% and a optical-to-microwave efficiency of 3.7%. These are several orders of magnitude larger than in our earlier work [10].

This class of device can be operated in the quantum regime, as ideal internal efficiencies approaching the ideal value are achievable, including increased G_{me} , better frequency-matched modes, and quality factors similar to those achieved for similar but incomplete devices. Future experiments will focus on cryogenic operation, further improvements to efficiency, and coupling to superconducting qubits.

Acknowledgments We thank P. J. Duda for fabrication assistance and F. Joseph Heremans and Nazar Delean for help with the AlN sputter system. The devices and experiments were supported by the Air Force Office of Scientific Research and the Army Research Laboratory. K.J.S. was supported by the National Science Foundation Graduate Research Fellowship Program (NSF-GRFP) (Grant No. NSF DGE-1144085), É.D. was supported by Laboratory Directed Research and Development Program (LDRD) funds from the Argonne National Laboratory; A.N.C. was supported in part by the U.S. Department of Energy (DOE), Office of Basic Energy Sciences. This work was partially supported by the University of Chicago Materials Research Science and Engineering Center (MRSEC) (Grant No. NSF DMR-1420709) and made use of the Pritzker Nanofabrication Facility, which receives support from SHyNE, a node of the NSF's National Nanotechnology Coordinated Infrastructure (Grant No. NSF NNCI-1542205).

The authors declare no competing financial interests. Correspondence and requests for materials should be addressed to A. N. Cleland (anc@uchicago.edu).

- [1] M. Kjaergaard, M. E. Schwartz, J. Braumüller, P. Krantz, J. I.-J. Wang, S. Gustavsson, and W. D. Oliver, Superconducting qubits: Current state of play, *Ann. Rev. Condens. Matter Phys.* **11**, 369 (2020).
- [2] F. Arute *et al.*, Quantum supremacy using a programmable superconducting processor, *Nature* **574**, 505 (2019).
- [3] H. J. Kimble, The quantum internet, *Nature* **453**, 1023 (2008).
- [4] N. Lauk, N. Sinclair, S. Barzanjeh, J. P. Covey, M. Saffman, M. Spiropulu, and C. Simon, Perspectives on quantum transduction, *Quantum Sci. Technol.* **5**, 020501 (2020).
- [5] N. J. Lambert, A. Rueda, F. Sedlmeir, and H. G. L. Schwefel, Coherent conversion between microwave and optical photons—An overview of physical implementations, *Adv. Quantum Technol.* **3**, 1900077 (2020).
- [6] L. Fan, C.-L. Zou, R. Cheng, X. Guo, X. Han, Z. Gong, S. Wang, and H. X. Tang, Superconducting cavity electro-optics: A platform for coherent photon conversion between superconducting and photonic circuits, *Sci. Adv.* **4**, eaar4994 (2018).
- [7] J. Bochmann, A. Vainsencher, D. D. Awschalom, and A. N. Cleland, Nanomechanical coupling between microwave and optical photons, *Nat. Phys.* **9**, 712 (2013).
- [8] R. W. Andrews, R. W. Peterson, T. P. Purdy, K. Cicak, R. W. Simmonds, C. A. Regal, and K. W. Lehnert, Bidirectional and efficient conversion between microwave and optical light, *Nat. Phys.* **10**, 321 (2014).
- [9] K. C. Balram, M. Davanco, J. D. Song, and K. Srinivasan, Coherent coupling between radio frequency, optical, and acoustic waves in piezo-optomechanical circuits, *Nat. Photon.* **10**, 346 (2016).
- [10] A. Vainsencher, K. J. Satzinger, G. A. Peairs, and A. N. Cleland, Bi-directional conversion between microwave

- and optical frequencies in a piezoelectric optomechanical device, *Appl. Phys. Lett.* **109**, 033107 (2016).
- [11] M. Forsch, R. Stockill, A. Wallucks, I. Marinković, C. Gärtner, R. A. Norte, F. v. Otten, A. Fiore, K. Srinivasan, and S. Gröblacher, Microwave-to-optics conversion using a mechanical oscillator in its quantum ground state, *Nat. Phys.* **16**, 69 (2020).
- [12] W. Jiang, C. J. Sarabalis, Y. D. Dahmani, R. N. Patel, F. M. Mayor, T. P. McKenna, R. V. Laer, and A. H. Safavi-Naeini, Efficient bidirectional piezo-optomechanical transduction between microwave and optical frequency, *Nat. Commun.* **11**, 1 (2020).
- [13] X. Han, W. Fu, C. Zhong, C.-L. Zou, Y. Xu, A. A. Sayem, M. Xu, S. Wang, R. Cheng, L. Jiang, and H. X. Tang, Cavity piezo-mechanics for superconducting-nanophotonic quantum interface, *Nat. Commun.* **11**, 3237 (2020).
- [14] A. P. Higginbotham, P. S. Burns, M. D. Urmey, R. W. Peterson, N. S. Kampel, B. M. Brubaker, G. Smith, K. W. Lehnert, and C. A. Regal, Harnessing electro-optic correlations in an efficient mechanical converter, *Nat. Phys.* **14**, 1038 (2018).
- [15] K. J. Satzinger, Y. P. Zhong, H.-S. Chang, G. A. Peairs, A. Bienfait, M.-H. Chou, A. Y. Cleland, C. R. Conner, E. Dumur, J. Grebel, I. Gutierrez, B. H. November, R. G. Povey, S. J. Whiteley, D. D. Awschalom, D. I. Schuster, and A. N. Cleland, Quantum control of surface acoustic wave phonons, *Nature* **563**, 661 (2018).
- [16] A. Bienfait, K. J. Satzinger, Y. P. Zhong, H.-S. Chang, M.-H. Chou, C. R. Conner, E. Dumur, J. Grebel, G. A. Peairs, R. G. Povey, and A. N. Cleland, Phonon-mediated quantum state transfer and remote qubit entanglement, *Science* **364**, 368 (2019).
- [17] L. R. Sletten, B. A. Moores, J. J. Viennot, and K. W. Lehnert, Resolving Phonon Fock States in a Multimode Cavity with a Double-Slit Qubit, *Phys. Rev. X* **9**, 021056 (2019).
- [18] Y. Chu, P. Kharel, T. Yoon, L. Frunzio, P. T. Rakich, and R. J. Schoelkopf, Creation and control of multi-phonon Fock states in a bulk acoustic-wave resonator, *Nature* **563**, 666 (2018).
- [19] I. Marinkovic, A. Wallucks, R. Riedinger, S. Hong, M. Aspelmeyer, and S. Gröblacher, An Optomechanical Bell Test, *Phys. Rev. Lett.* **121**, 220404 (2018).
- [20] R. Riedinger, A. Wallucks, I. Marinkovic, C. Löschnauer, M. Aspelmeyer, S. Hong, and S. Gröblacher, Remote quantum entanglement between two micromechanical oscillators, *Nature* **556**, 473 (2018).
- [21] M. Wu, E. Zeuthen, K. C. Balram, and K. Srinivasan, Microwave-to-Optical Transduction Using a Mechanical Supermode for Coupling Piezoelectric and Optomechanical Resonators, *Phys. Rev. Appl.* **13**, 014027 (2020).
- [22] M. Eichenfield, J. Chan, R. M. Camacho, K. J. Vahala, and O. Painter, Optomechanical crystals, *Nature* **462**, 78 (2009).
- [23] S. M. Meenehan, J. D. Cohen, G. S. MacCabe, F. Marsili, M. D. Shaw, and O. Painter, Pulsed Excitation Dynamics of an Optomechanical Crystal Resonator near its Quantum Ground-State of Motion, *Phys. Rev. X* **5**, 041002 (2015).
- [24] G. S. MacCabe, H. Ren, J. Luo, J. D. Cohen, H. Zhou, A. Sipahigil, M. Mirhosseini, and O. Painter, Phononic bandgap nano-acoustic cavity with ultralong phonon lifetime, [arXiv:1901.04129](https://arxiv.org/abs/1901.04129).
- [25] A. H. Safavi-Naeini and O. Painter, in *Cavity Optomechanics*, edited by M. Aspelmeyer, T. J. Kippenberg, and F. Marquardt (Springer, Berlin, 2014), p. 195.
- [26] M. Aspelmeyer, T. J. Kippenberg, and F. Marquardt, Cavity optomechanics, *Rev. Mod. Phys.* **86**, 1391 (2014).
- [27] C. Genes, D. Vitali, P. Tombesi, S. Gigan, and M. Aspelmeyer, Ground-state cooling of a micromechanical oscillator: Comparing cold damping and cavity-assisted cooling schemes, *Phys. Rev. A* **77**, 033804 (2008).
- [28] V. Laude, D. Gérard, N. Khelifaoui, C. F. Jerez-Hanckes, S. Benchabane, and A. Khelif, Subwavelength focusing of surface acoustic waves generated by an annular interdigital transducer, *Appl. Phys. Lett.* **92**, 094104 (2008).
- [29] D. M. Pozar, *Microwave Engineering* (Wiley, NY, 2012), 4th ed.